Int J Adv Manuf Technol (2018) 94:3949–3961
DOI 10.1007/s00170-017-1128-x

ORIGINAL ARTICLE

Mechanical properties of Inconel 718 welds performed by gas tungsten arc welding

R. Cortés[1,2] · **E. R. Barragán**[1] · **V. H. López**[2] · **R. R. Ambriz**[1] · **D. Jaramillo**[1]

Received: 18 April 2017 / Accepted: 13 September 2017 / Published online: 26 September 2017

Abstract Gas tungsten arc welding (GTAW) was used to join plates of Inconel 718. The mechanical properties were determined by tensile, microhardness, and instrumented Charpy impact tests. An ERNiFeCr-2 filler metal fed by a semi-automatic mechanism was used. Partial dissolution of the strengthening phases, γ' and γ'', induced a soft region (~ 225 $HV_{1.0}$) in the heat-affected zone (HAZ) during welding. The yield strength (371.3 MPa) of the as-welded joint is approximately 45% of the base material in aged condition (822.7 MPa). The welds were subjected to a hardening recovery post weld heat treatment (HRPWHT). Impact testing of the hardened welds revealed a reduction of 17% in energy absorbed with respect the aged base material. Hardness measurements showed an increase to ~ 410 $HV_{0.1}$ in the fusion zone; however, due to segregation of Nb and formation of carbides, the precipitation of γ'' is not fully completed, and the yield strength (719 MPa) of the heat-treated welded joint is lower than the base material in aged condition.

Keywords Inconel 718 · GTAW · Mechanical properties · Post weld heat treatment

✉ R. R. Ambriz
rrambriz@ipn.mx

[1] Instituto Politécnico Nacional CIITEC-IPN, Cerrada de Cecati S/N Col. Sta. Catarina, 02250 Azcapotzalco, CDMX, Mexico

[2] Instituto de Investigación en Metalurgia y Materiales, Universidad Michoacana de San Nicolás de Hidalgo, A.P. 888, 58000 Morelia, MICH, Mexico

1 Introduction

Ni-Cr-Fe alloys are sought after in a number of applications in aircraft, power generation, and petrochemical industries due to their excellent mechanical properties at cryogenic and high temperatures as well as corrosion resistance in aggressive environments. The Ni-Cr-Fe alloys hardened by precipitation are used when corrosion resistance and mechanical strength at high temperatures are demanded [1]. In virtue of these characteristics, the engineering applications of Ni-Cr-Fe alloys have been increasing and, as a consequence, its welding metallurgy has become an active field of research, especially because these materials are used in paramount components of gas turbines in aeronautic, nuclear power, oil, and food industries [2, 3].

Several welding processes may be used for welding Ni-Fe-Cr alloys. However, engineers must be aware of some metallurgical issues related to the fusion zone (FZ) and HAZ. While solidification cracking and undesirable secondary phases precipitation are the most important weldability problems in the FZ; liquation cracking, Laves phase precipitation, δ phase, and carbides formation in the HAZ are the main concerns in the reliability of the welded joints. For instance, precipitation of secondary phases in Inconel 718 (IN718) occurs by the segregation of Nb and Mo during solidification; this behavior is promoted by the content of Fe in the matrix [1]. Additionally, the presence of Laves phase and NbC in the welded joints leads to low strength and reduced ductility in the FZ making this zone prone to failure [4]. Furthermore, the precipitation of NbC in the HAZ reduces the content of Nb available for the formation of the strengthening γ'' phase [5]. Even if the IN718 welds are subjected to an annealing treatment, the presence of NbC is not suppressed because these carbides

precipitate again during the aging treatment [6]. Another factor that decreases the mechanical properties of the welded joint is the reversion of precipitates in the HAZ where the γ' and γ'' phases partially dissolve due to the temperatures experienced during welding [7].

This study deals with the microstructural characteristics and mechanical properties of IN718 GTAW welded joints. The results are comparatively reported for the as-welded and post weld heat-treated welded joints. A glance to the open literature shows that the information concerning the welding metallurgy and mechanical behavior of IN718 welds is lacking.

2 Methodology

2.1 Materials and welding

An Inconel 718 plate of 1500 × 300 × 6.35 mm was used. The material was supplied in annealed condition with the following mechanical properties: Vickers hardness number of 236.4 ± 5.2, yield strength of 430.3 ± 5.7 MPa, tensile strength of 842.9 ± 15.3 MPa, and elongation of 51.4 ± 0.7%. Metallographic samples of 60 × 10 × 6.35 mm of base material were mirror polished using conventional techniques. The microstructure was revealed by immersion of the samples in a solution of 67% HCl + 33% HNO_3. Optical microscopy was used to analyze the structure of the material and the different zones of the welded joints. The chemical composition of the base and filler metals as determined by optical emission spectroscopy is shown in Table 1.

Plates of 150 × 75 × 6.35 mm of base material were machined to obtain a single V-groove joint according to the dimensions indicated in Fig. 1.

The plates were hardened by precipitation prior to welding, which is the typical condition for using the IN718 alloy. The plates were solution heat treated at 1065 °C for 1 h followed by cooling in atmospheric air. Subsequently, the plates were aged at 720 °C for 8 h and finally furnace cooled. This heat treatment provided a Vickers hardness number of 408.5 ± 3.2, yield strength of 822.7 ± 9.6 MPa, tensile strength of 1090.3 ± 4.6 MPa, and elongation of 41.2 ± 3.9%. After welding, in order to restore and increase the strength in the HAZ and FZ, respectively, some welded joints were subjected to an HRPWHT as detailed above for the IN718 plates.

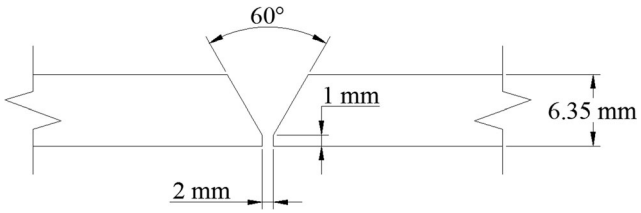

Fig. 1 Design and dimensions of the single V-groove joint used

A semi-automatic gas tungsten arc welding (GTAW) process was used (Fig. 2) to weld the IN718 plates. An ER NiFeCr-2 filler wire, 1.1 mm in diameter, was fed by a semi-auto mechanism at 170 mm s^{-1}. The GTAW torch was set at approximately 15° with respect to the normal of the plates and displaced at 4 mm s^{-1}. A mixture of H_2 (2%), CO_2 (0.12%), He (30%), and Ar (67.88%) was used as shielding gas flowing at 16.50 dm^3 min^{-1}. Alternating current and tungsten-thorium electrode were used with a potential of 29 V and current of 356 A. These parameters provided a heat input of 1806.7 J mm^{-1}, considering a thermal efficiency of 70%.

2.2 Macro and microstructural characteristics of the welded joints

The optical and scanning electron microscopes were used to analyze the microstructure of the welded joints in the as-welded and HRPWHT conditions. The mechanical properties of the welds were determined by means of microhardness measurements, tensile, and instrumented Charpy impact tests.

Transversal welding profiles were cut from the welded joints for microstructural analysis. The FZ, partially melted zone (PMZ), and HAZ were analyzed to determine the microstructural characteristics of the welds. Additionally, energy dispersive X-ray spectroscopy (EDX) was used to determine the chemical composition of the matrix and some secondary phases. This technique was also used to obtain elemental concentration maps in some areas to observe the distribution of certain elements.

2.3 Evaluation of mechanical properties

Vickers microhardness measurements (maps and profiles) were performed to analyze the local variations in hardness across the welded joints. The indentations were made by applying a load of 1.0 kg (9.81 N) during 15 s. The

Table 1 Chemical composition of the materials used (wt. %)

Material	C	Cr	Fe	Mn	Ni	Mo	Ti	Al	Other
IN718*	0.05	18.3	19.34	0.08	52.7	2.9	1.03	0.58	5.02 Nb
ERNiFeCr-2*	0.05	17.7	20.3	0.08	51.7	3.1	0.98	0.45	5.45 Nb

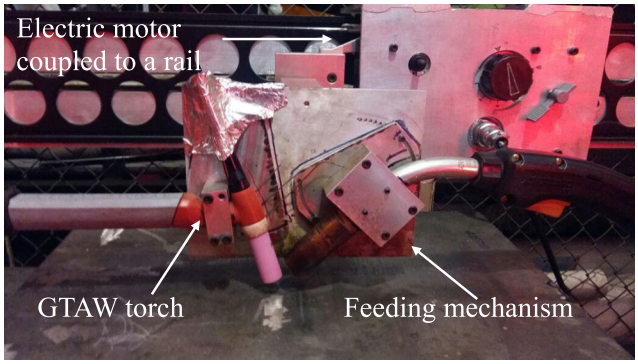

Fig. 2 Semi-automatic GTAW process

impressions were carried out in linear profiles separated by 1 mm between one and another, the distance between indentations was 500 μm and the length of the profiles was ~ 25 mm (12.5 mm from the center of the weld bead to both sides). The information was processed by using OriginPro 8 ® to obtain the mapping representation of the hardness variations across the welds.

Tensile testing of the welded joints was performed on standard subsize specimens, according to ASTM E8M-04 [8]. The cross-head travel speed was 1 mm min^{-1}. The length increment during testing was measured with an extensometer placed in a gauge length of 25 mm. To determine the strain hardening exponent, *n*, and the strength coefficient, *H*, the recommendations of the ASTM E646-16 standard [9] were fulfilled. The fracture surfaces obtained from tensile tests were analyzed to correlate the morphology of the fracture and to obtain information about fracture mechanisms.

An instrumented Charpy impact device was used to determine the impact resistance of the welded joints. Subsize specimens (5 × 10 × 55 mm) were machined according to the ASTM E23-02A standard [10]. The V notch was aligned on the FZ for the welds in both conditions (as-welded and HRPWHT). The results obtained were compared with those for the base material. The samples were taken from the transverse direction of the weld bead. The data were treated according to the ASTM E2298-15 standard [11].

3 Results and discussion

3.1 Microstructure of the base metal

The characteristic microstructure of the IN718 alloy in annealed and aged conditions is shown in Fig. 3. An austenitic matrix, γ, with equiaxed grains and the presence of twinning was observed. This microstructure was produced by the mechanical deformation during rolling and annealing treatment. Twinning is typical in annealed alloys with FCC crystallographic structure [12]. Additionally, it is possible to observe, under the resolution of the optical microscope, the presence of carbides randomly dispersed in the austenitic matrix. The IN718 alloy was received in annealed condition, which promotes the distribution of the alloying elements within the matrix. However, the optical micrographs reveal that this metallurgical condition is not fully completed as evidenced by the presence of carbides observed in both conditions, aged and annealed.

In the aged condition, Fig. 3b, it is possible to observe a major presence of MC-type precipitates (where M may be Ti or Nb or even both), MoC and M_6C (where M may be Fe, Cr, Mo, W, and Nb) as compared to the annealing condition (Fig. 3a). This observation is supported by the results obtained from the composition dot maps shown in Fig. 4. In these images, it is possible to evidence the concentration of these elements in the particles seen in the micrograph in secondary electron mode shown in Fig. 4a.

The presence of these secondary phases is produced as a result of the segregation of Nb and Mo during solidification [1]. Also, due to the partition of these elements, formation of Laves phase is likely to take place. The precipitation of Laves is promoted by the content of Fe in the austenitic matrix [13–15].

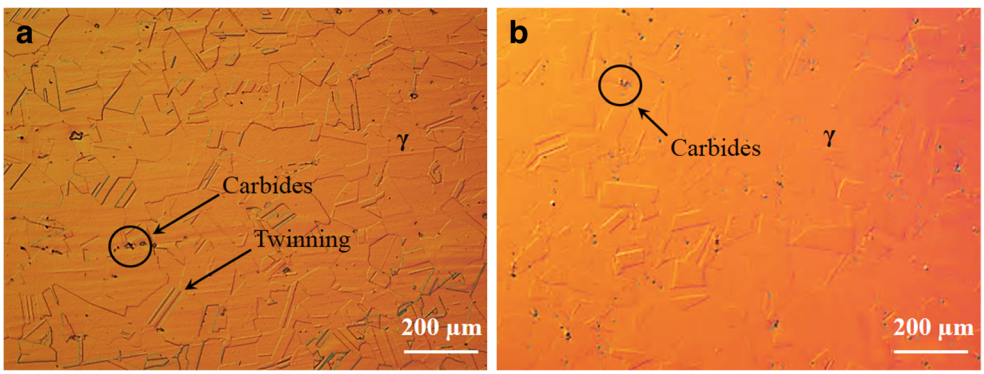

Fig. 3 Microstructure of the IN718 alloy in **a** annealed and **b** aged conditions

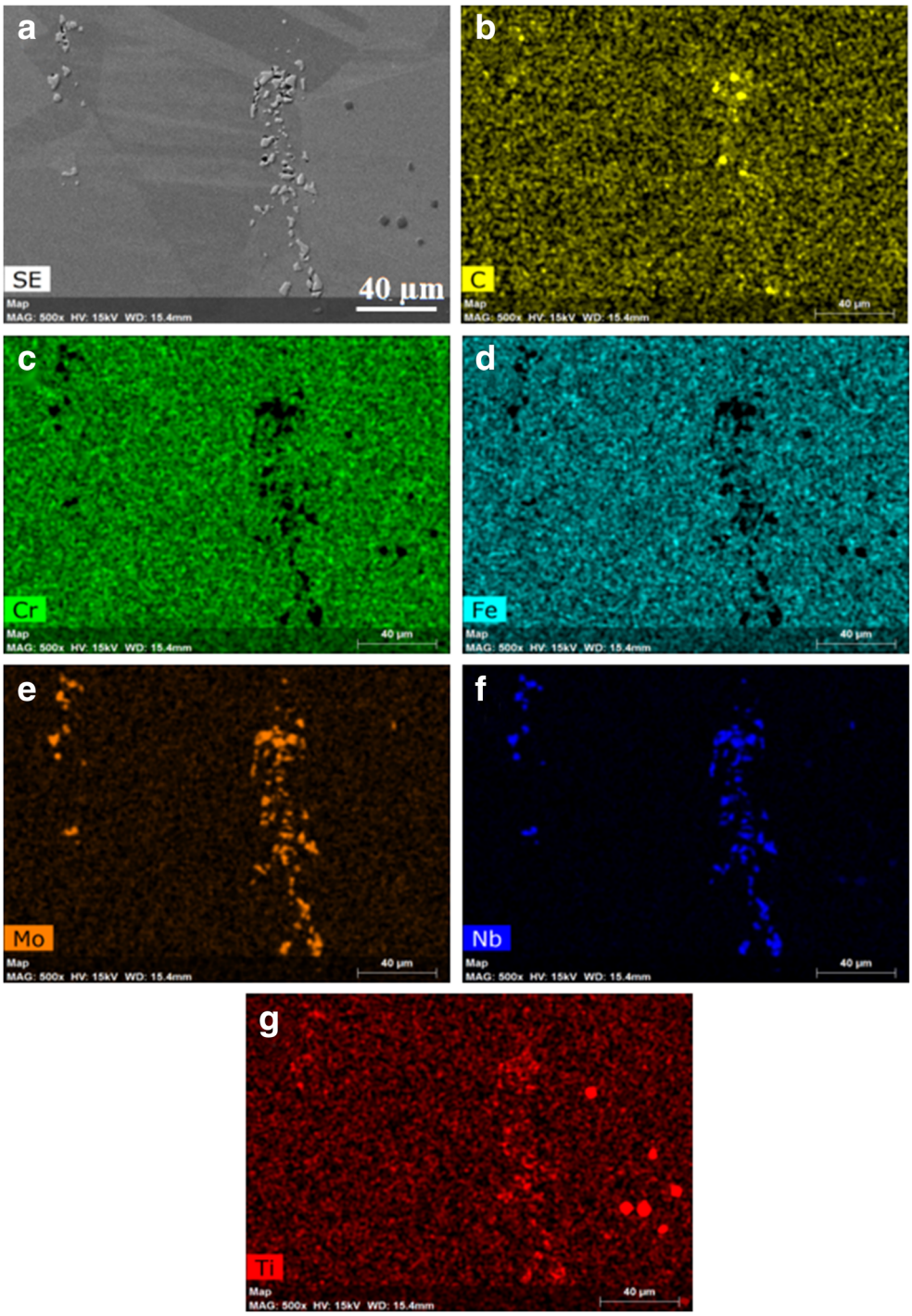

Fig. 4 Elemental concentration in an optical field of IN718 in aged condition

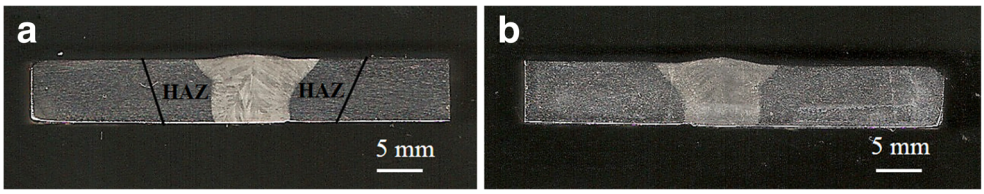

Fig. 5 Transverse view of the welded joints in **a** as-welded and **b** HRPWHT conditions

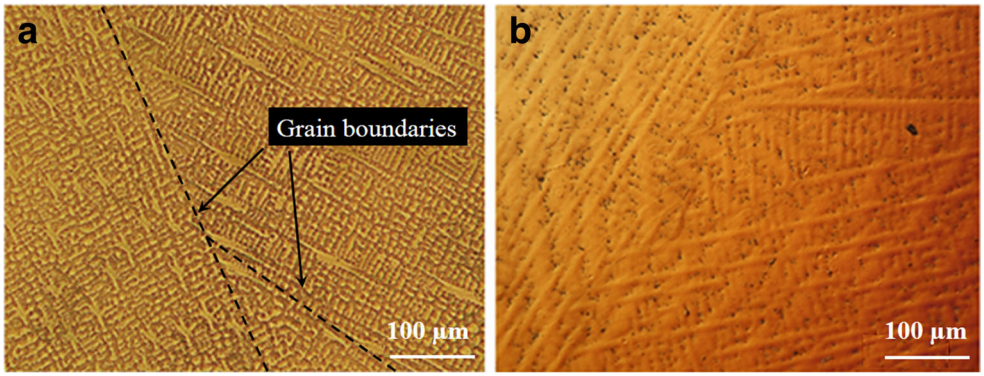

Fig. 6 Microstructure in the middle of the fusion zone. **a** As-welded and **b** with HRPWHT

3.2 Macro and microstructural characteristics of the welded joints

Figure 5 shows the welding profiles obtained from IN718 plates in the as-welded (Fig. 5a) and HRPWHT (Fig. 5b) conditions. As can be observed, the welded joints exhibit an adequate welding bead geometry with complete penetration and without lack of lateral fusion. Also, no visible inclusions, spatter, or distortion were observed.

The microstructure in the FZ of the welds in the as-welded and HRPWHT conditions is presented in Fig. 6. The typical columnar dendritic structure is appreciated in both conditions. Also, traditional columnar competitive growth can be observed, which is produced by the reorientation of dendrites, which tend to grow preferentially on the <100> directions [16], i.e., the crystallographic growth in FCC structure (IN718).

In order to ascertain the presence of Nb and Mo segregated during the solidification, an elemental concentration map on the dendritic columnar structure in the middle of the FZ was performed as shown in Fig. 7. The segregation of these elements is highlighted by the bright areas in Fig. 7e and f that represent the zones with more concentration of Nb and Mo, respectively. The partition of these elements gives rise to the precipitation of secondary phases (Laves in the case of Nb) and to Mo depleted zones that make the weld metal prone to localized corrosion.

Figure 8 shows the microstructure at the interface formed between the FZ and HAZ of the welds in both welding conditions. The FZ and HAZ are clearly delimited by the partially melted grains in the base material. The welds exhibit epitaxial growth, which means that the dendrites grow in a different direction depending on the orientation of the grains in the base material [17]. An increment of secondary phases in the HAZ and FZ was observed after the HRPWHT. EDX punctual microanalyses and dot maps confirmed the presence of Nb, Ti, and Mo carbides in these zones as shown in Fig. 9. Only one elemental concentration map is presented, but the analyses performed to the other particles in both samples exhibited similar results.

The increment of carbides in the HAZ and FZ may be attributed to the strong tendency of carbon to segregate towards the liquid during solidification, allowing the formation of carbides. Besides, carbon has a high diffusivity in solid state in a Ni-based austenitic matrix. Thus, C diffuses from the FZ to the HAZ and reacts with some alloying elements forming carbides in addition to those already present in the alloy [2, 18].

Figure 10 shows the microstructure of the HAZ. Figure 10a and b corresponds to the HAZ in as-welded and HRPWHT conditions, respectively. Figure 9 confirmed the presence of secondary phases rich in Mo, Nb, Ti, and C, most likely corresponding to carbides. Although the sample shown in Fig. 10b was subjected to solution heat treatment at 1065 °C for 1 h followed by and aging at 720 °C, the quantity of precipitates in the HAZ did not decrease significantly. Thus, solution heat treatment dissolves part of these carbides, but they tend to precipitate again due to the aging treatment [6].

3.3 Variations in microhardness in the welded joints

The Vickers hardness number of the base material IN718 in annealed and aged conditions was 236.4 ± 5.2 and 408.5 ± 3.2, respectively. This increment in hardness was the response to the heat treatment, solubilization, and aging, resulting in the precipitation of the hardening γ'' and γ' phases [19]. In order to establish the variation in hardness along the weld profile in the as-welded and HRPWHT conditions, microhardness profiles and mapping representation were plotted as illustrated in Fig. 11. In these images, it is possible to identify the FZ, HAZ, and BM. In the as-welded condition (Fig. 11a and c), an important decrement of approximately 150 units in hardness at the FZ and at the HAZ was observed with respect to the base material in aged condition. In the case of the FZ, the factor that contributes to the low hardness is the Nb segregation during solidification, favoring the precipitation of NbC and decreasing the amount of Nb for the formation of the γ'' phase [5]. Regarding the HAZ, the reduction in hardness was associated to the partial dissolution of the secondary phases in the region adjacent to the FZ. The peak

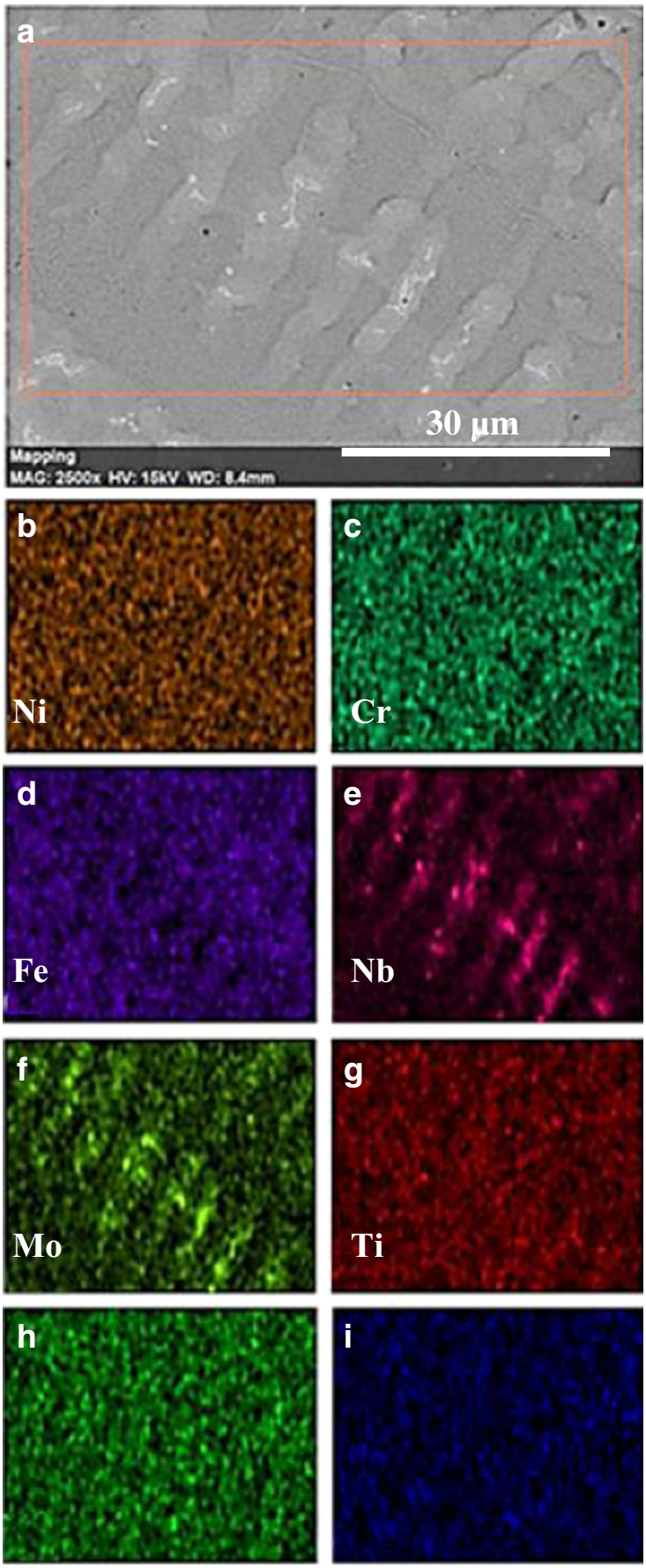

Fig. 7 Elemental concentration map in a dendritic structure in the FZ of a welded joint in the as-welded condition

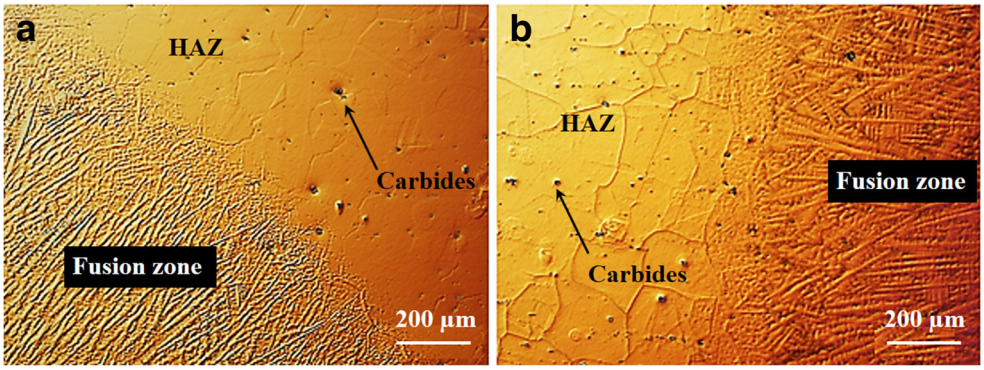

Fig. 8 Microstructure at the FZ/HAZ interface in **a** as-welded and **b** HRPWHT conditions

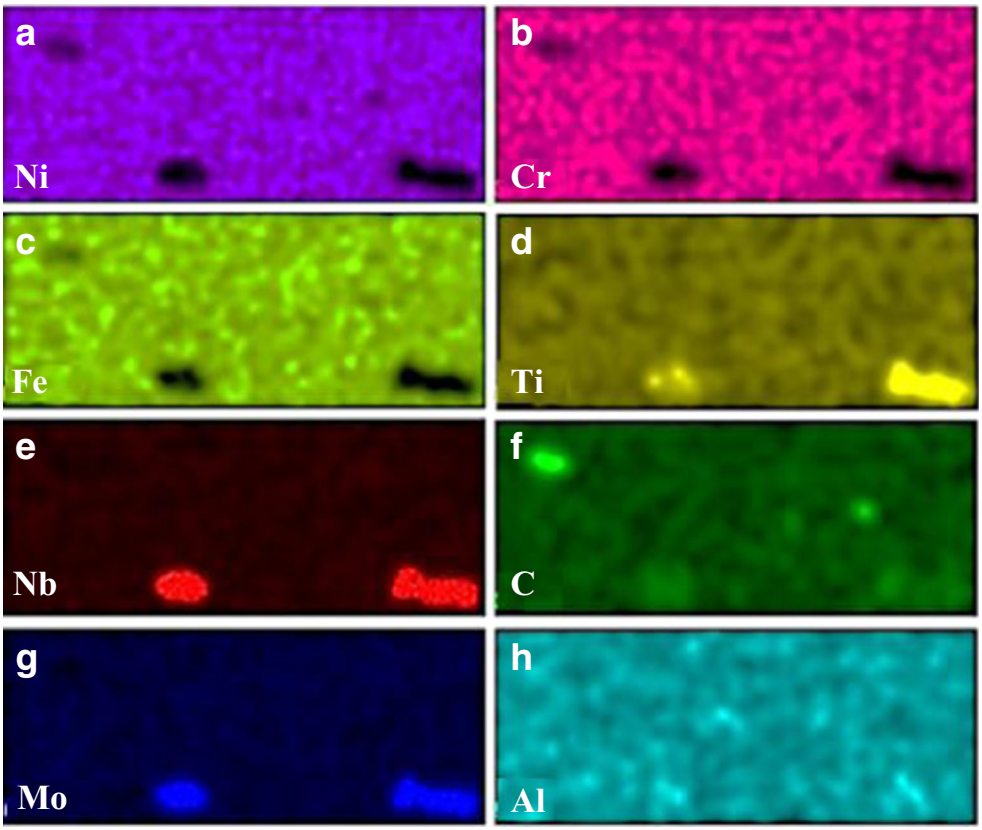

Fig. 9 Elemental concentration map of particles in the HAZ after HRPWHT

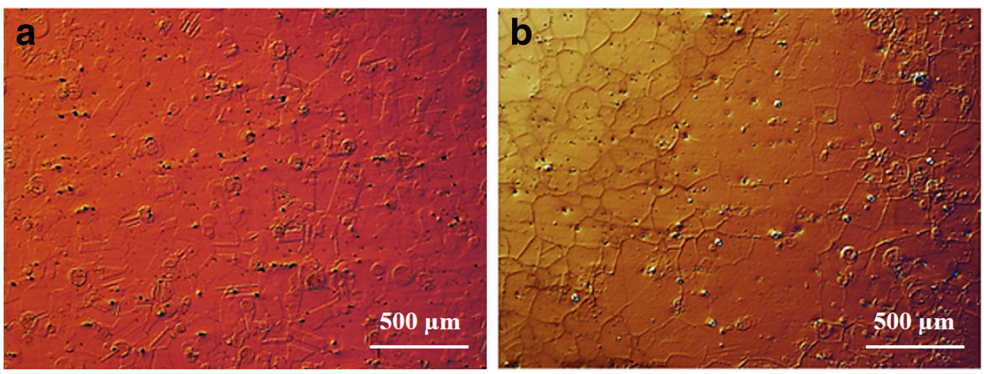

Fig. 10 Microstructure in the HAZ in **a** as-welded and **b** HRPWHT conditions

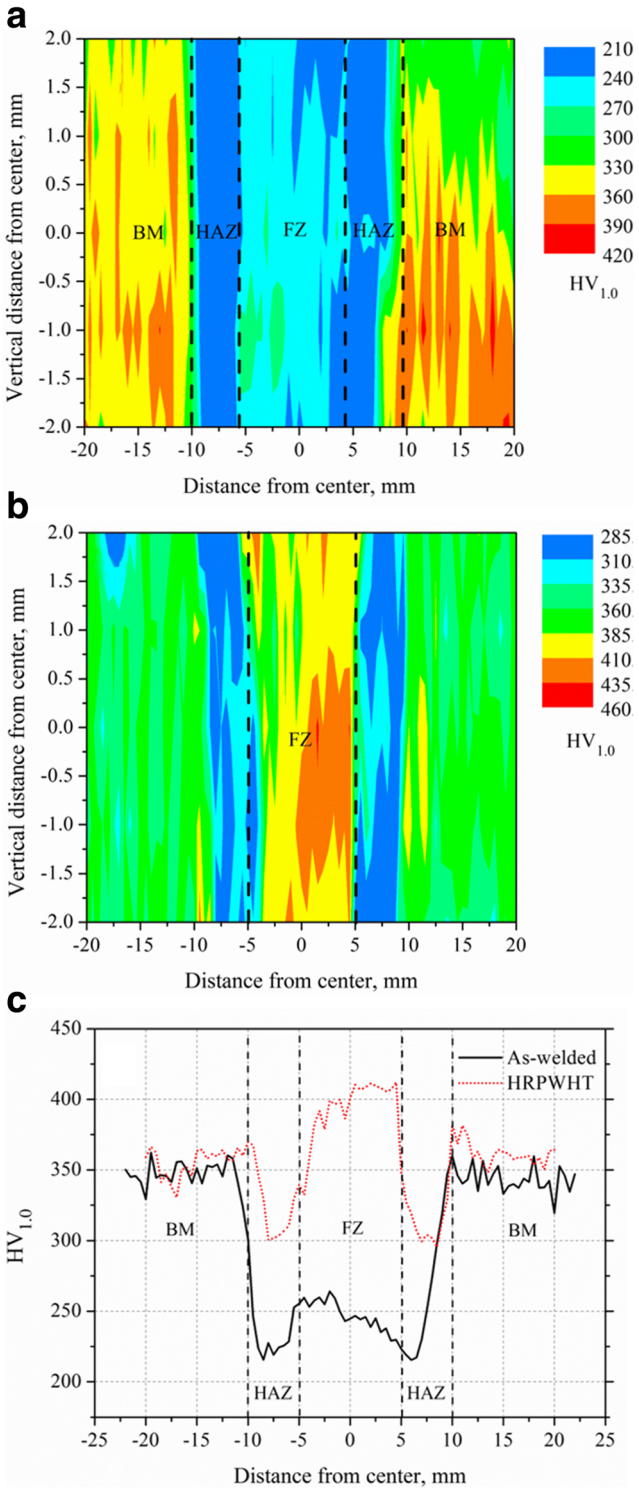

Fig. 11 Hardness distribution in the welded joints. **a** and **b** microhardness maps for the as-welded and HRPWHT conditions, respectively and **c** comparison of microhardness profiles for both welds

temperature in this zone is higher than the precipitation temperature of the γ′ and γ″ phases leading thus to its complete or partial dissolution. This behavior was previously observed by Hirose et al. [7].

Figure 11b and c shows the hardness distribution of IN718 welded plates subjected to the HRPWHT. From the microhardness profile, it is possible to observe that the FZ has a similar level in hardness as compared to the base material in aged condition. In spite of the increase in hardness in the FZ and HAZ with respect to the as-welded condition, the values were still lower than the average value measured in the base material. Even when the samples were subjected to solution heat treatment, NbC precipitated during the aging process. Also, the segregation of Nb is not suppressed because it is considered that the solid-state diffusion of substitutional elements is very limited [1]. The partition of Nb and the consequent precipitation of NbC are associated with the loss of the strengthening γ″ phase [5] which is reflected in a reduction in the hardness of these zones. The amount of these secondary phases, formed during the HRPWHT, is not enough to achieve the average hardness values of the base material in aged condition. In this context, it is reasonable to expect that certain amount of the Nb present in the austenitic matrix was consumed by the precipitation of NbC during the prolonged holding time at 720 °C, limiting thus the extent of hardening and recovery in this zone.

3.4 Tensile strength of the welded joints

Conventional stress-strain behavior of IN718 in annealed and aged conditions is shown in Fig. 12a whereas Fig. 12b plots the curves for the welded joints in the as-welded and HRPWHT conditions. A summary of the results obtained from these tests is listed in Table 2. Tensile properties in longitudinal (L) and transverse (T) to rolling direction were determined for the annealed condition. The stress-strain behavior in both directions are very similar; this behavior was promoted by the annealing treatment, as it produces the homogenization of the microstructure. In response to the aging heat treatment, an outstanding increment in tensile properties has been obtained in the IN718 alloy as a result of the formation of γ′ and γ″ secondary phases. This hardening is produced because the dislocations in the material need more force to cut the γ′ precipitates along with the strain produced by the γ″ phase in the FCC austenitic matrix. The BCT crystal structure of the γ″ phase is coherent with the FCC austenitic matrix. The strain generated by the lattice mismatch, ~ 3%, between γ and γ″, increases the mechanical resistance at low temperatures in this alloy [1].

Tensile behavior of the welded joints is shown in Fig. 12b. A ductile failure was exhibited for the as-welded condition. Although the samples presented the necking phenomenon in the HAZ due to the plastic deformation, failure took place in the FZ. It was observed that this area did not present an evident plastic deformation as seen in the HAZ. This behavior is not consistent with

Table 2 Tensile properties obtained from stress-strain curves of IN718

Material	σ_0 (MPa)	σ_{max} (MPa)	Fracture energy (MJ m^{-3})	Number (n)	H (MPa)	Elongation (%)
IN718 annealed	430.3 ± 5.7	842.9 ± 15.3	387.7 ± 12.7	0.26	1467.8	51.4 ± 0.7
IN718 aged	822.7 ± 9.6	1090.3 ± 4.6	434 ± 5.1	0.12	1482.0	41.2 ± 3.9
IN718 as-welded	371.3 ± 12.3	660.0 ± 13.49	147.6 ± 26.13	0.31	1304.3	25.7 ± 3.7
IN718 HRPWHT	719.0 ± 39.0	988.0 ± 12	246.6 ± 10.7	0.20	1640.6	26.9 ± 2.4

σ_0 yield strength, σ_{max} tensile strength, n strain hardening exponent, H strength coefficient

hardness results obtained for this condition, because the lowest hardness values were obtained at the HAZ and fracture was expected to occur in this zone of the welded joint, i.e., the tensile specimens failed in the FZ due to the presence of brittle secondary phases which acted as crack nucleating agents. A similar behavior was reported by Hirose et al. [4]. The tensile strength (~ 660 MPa) and yield strength (~ 371 MPa) were lower than the base material in the annealed condition. This decrement, as pointed for hardness variations, is likely due to segregation of Nb during the solidification of the weld pool and the subsequent formation of NbC. This microstructural feature decreases the content of Nb available for the formation γ'' phase in the FZ and PMZ. These findings are consistent with the studies of Hinojos et al. [5].

The conventional stress-strain behavior for the welds subjected to HRPWHT is shown in Fig. 12b. It is evident that yield (~ 719 MPa) and tensile strength (~ 988 MPa) values are slightly lower than the base material in aged condition. In this instance, the tensile specimens failed in the HAZ, where necking due to the plastic deformation was seen and the soft region across the welded joint was located according to hardness measurements. Even when a solution heat treatment and age hardening [20] were given to the welded joints, the tensile mechanical properties were lower than the base material in aged condition. This issue has been previously explained in terms of Nb segregation and the posterior formation of carbides, which tend to diminish the Nb available for the formation of the strengthening γ'' phase [5].

In the as-welded and HRPWHT conditions, it was observed a serrated plastic behavior, which can be classified as type A or C (the geometry is similar, and it is not possible to differentiate the exact shape of serrations), according to the classification of Rodríguez [21], i.e., serrations that appear in a periodic way through the plastic zone in a stress-strain curve. The serrated plastic flow is described as an anomalous behavior, which is a common manifestation of the dynamic stress aging (DSA) phenomenon. The DSA is produced for the interaction between atoms of solute that diffuse and the mobile dislocations during the plastic deformation; it depends on the strain rate and temperature that define the mobility of the dislocations and the dilution of solute atoms, respectively. It has been found that the fatigue resistance of materials having an austenitic FCC

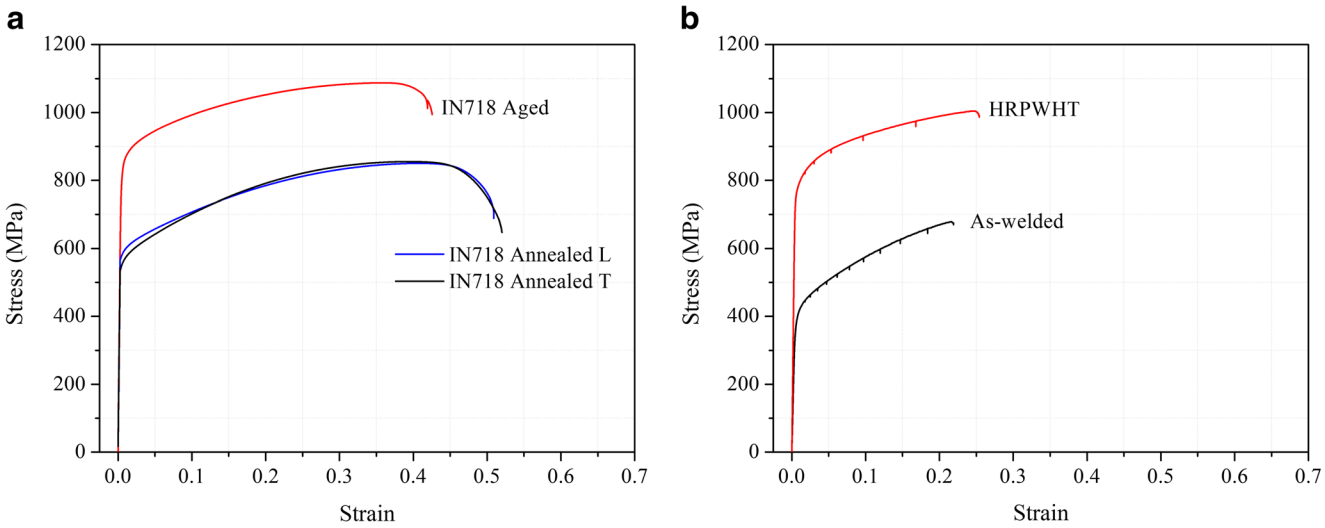

Fig. 12 Conventional stress-strain curves for **a** base material in annealed and aged conditions and **b** welded joints in the as-welded and HRPWHT conditions

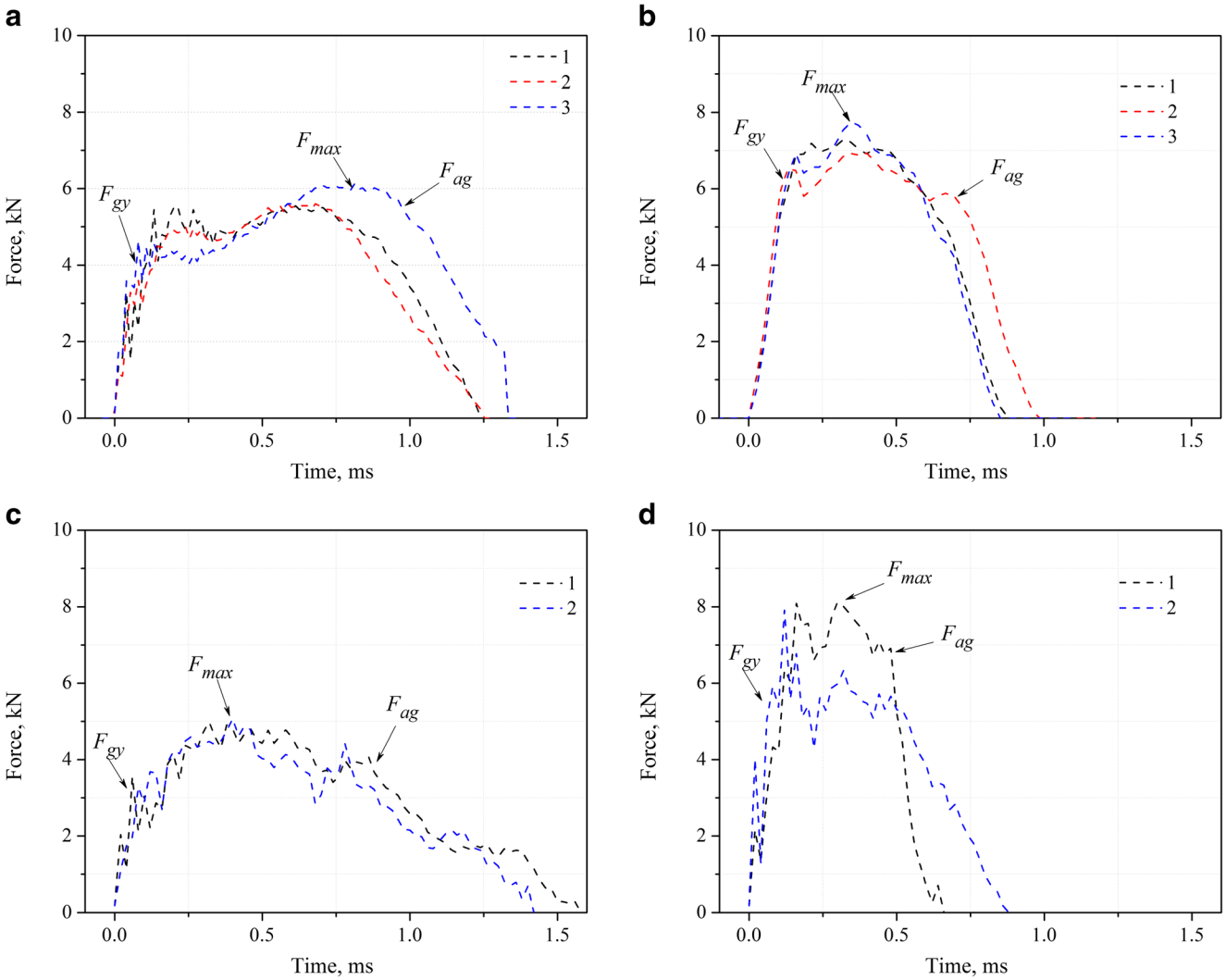

Fig. 13 Force-time curves obtained from instrumented impact Charpy tests for IN718, **a** annealed, **b** aged, **c** as-welded, and **d** HRPWHT

Table 3 Average fracture energy obtained from impact Charpy tests

Material condition	IN718 annealed	IN718 aged	IN718 as-welded	IN718 HRPWHT
Energy (MJ m^{-3})	12.8 ± 1.5	10.6 ± 0.5	10.5 ± 0.6	8.4 ± 0.5

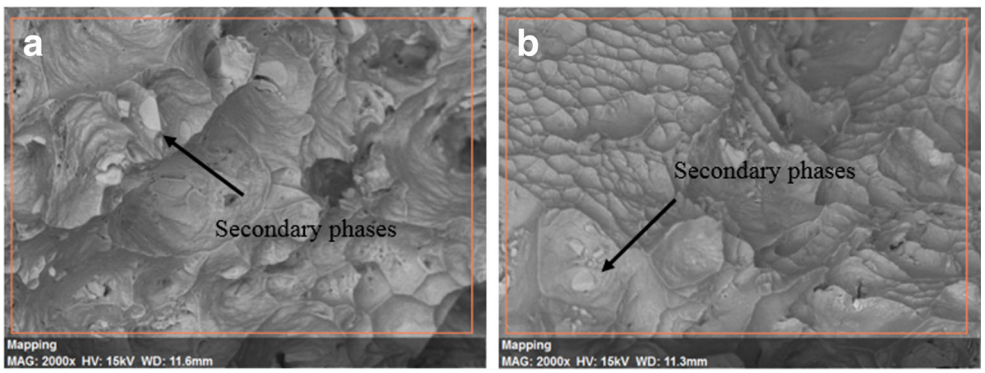

Fig. 14 Tensile fracture surfaces of the base material in **a** annealed and **b** aged conditions

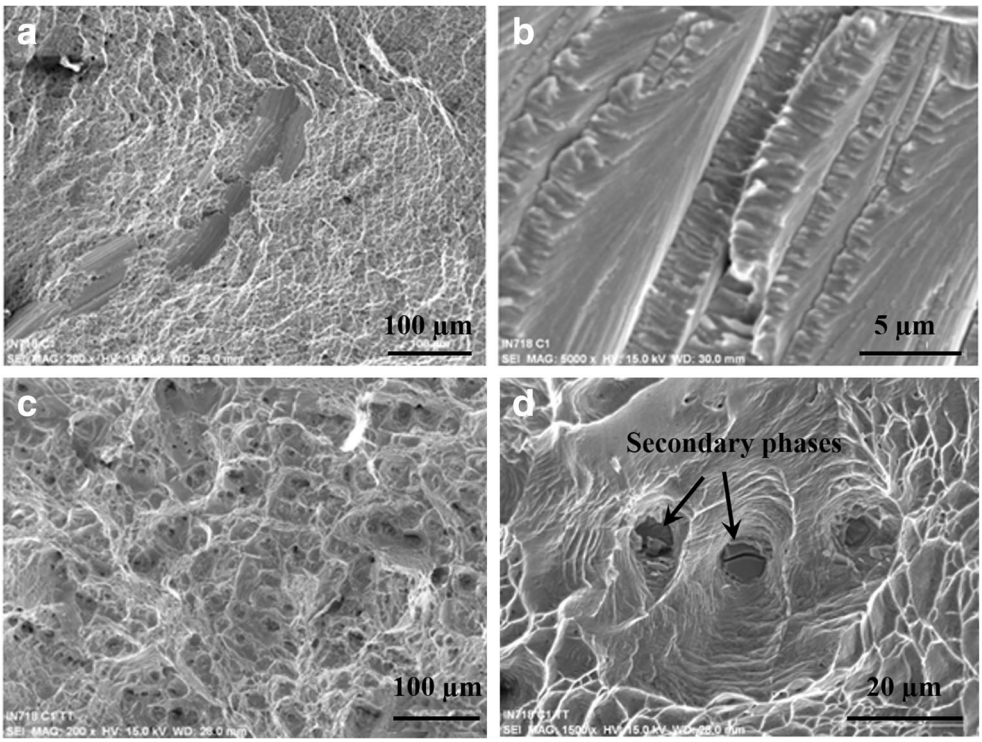

Fig. 15 Fracture surfaces at the fusion zone for welds in **a** and **b** as-welded condition and **c** and **d** with HRPWHT

matrix decreases due to the lack of homogeneity in the deformation and the hardening induced for the DSA [22, 23].

3.5 Impact resistance of the welded joints

Figure 13a and b show the force-time graphs obtained from instrumented impact Charpy tests on IN718 in annealed and aged conditions, respectively. Table 3 shows the average values of the absorbed fracture energy as measured from these graphs. Considering the ASTM E2298-15 standard, it is possible to observe a type C geometry, corresponding to a fully ductile behavior [11]. It is evident that yield force (F_{gy}), maximum force (F_{max}), and the force for unstable crack propagation (F_{ag}) in aged condition (Fig. 13b) are higher than those obtained for the annealed condition (Fig. 13a). However, it has been observed an improvement in terms of absorbed fracture energy for the annealed condition (Table 3), i.e., higher ductility than for the aged condition.

Figure 13c and d shows the force-time curves obtained in the FZ for the welded joints in the as-welded and HRPWHT conditions, respectively. A ductile behavior was observed in both conditions. The as-welded samples presented a reduction in terms of absorbed impact energy in comparison with the base material in annealed condition; this reduction was attributed to the brittle secondary phases formed during the welding process. Nevertheless, the samples in HRPWHT exhibited a lower impact resistance than for the as-welded condition. This aspect is mainly related to the hardness increment observed in Fig. 11, which shows that the FZ of the HRPWHT sample exhibits the highest hardness of the welded joint suggesting a brittle behavior in an impact. Despite the similitude in hardness values for the FZ in the HRPWHT sample and base metal in aged condition, the impact resistance of the welded joint is

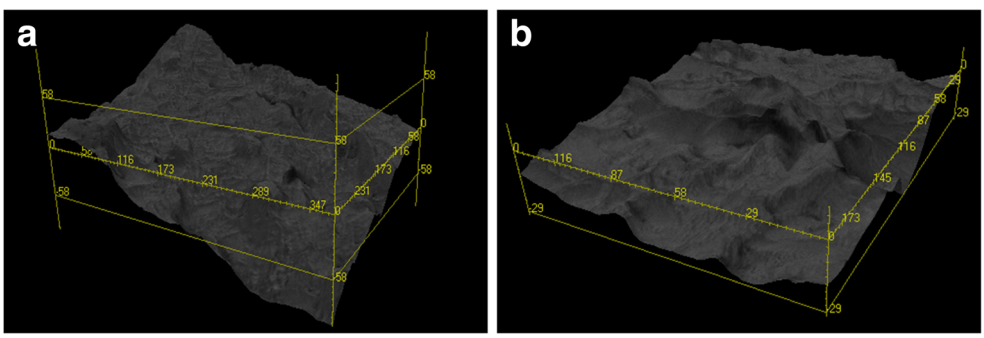

Fig. 16 Reconstruction in 3D of the topography of the IN718 fracture for specimens **a** annealed and **b** aged

lower. This is owing to the presence of the secondary Laves phase (brittle phase), which tends to produce detrimental effects on the mechanical properties [24].

3.6 Fracture surfaces

The fracture surfaces obtained from tensile tests for base material in annealed and aged conditions are shown in Fig. 14. A completely ductile fracture appearance was observed, which is characterized by the presence of microvoids formed during the deformation process, as well as the presence of secondary phases.

The fracture surfaces for the IN718 welds are shown in Fig. 15a and b. It is possible to observe ductile and fragile regions. It is believed that the brittle fracture was because of the presence of secondary phases such as Laves and δ.

The fracture was ductile for the samples with HRPWHT as shown in Fig. 15c and d. In the topography of the fractures, it is observed the presence of secondary phases. It is thought that these particles are Nb and Mo carbides as suggested by EDX analysis.

The fracture surface topography is shown with more details in the three-dimensional reconstruction presented in Fig. 16, where the presence of voids is evident as well as peaks of different size produced by plastic deformation in the material. Also, it is possible to observe the nucleation, growth, and coalescence of microvoids.

An EDX analysis in the surface of the fracture revealed the presence of Mo and Ti in the secondary phases. As it has been mentioned, the Nb and Mo tend to segregate during the solidification that is because these elements have a partition coefficient, k, lower than one, i.e., with the presence of Fe, this coefficient tends to be minor.

4 Conclusions

Microstructural characterization and mechanical evaluation of the welded joints revealed a significant reduction in mechanical strength due to the partial dissolution of the strengthening phases γ' and γ'' in the HAZ. The mechanical properties of the welded joints may be improved by hardening recovery provided by the post weld heat treatment. However, tensile strength and impact resistance are not fully restored due to the presence of brittle secondary phases such as Laves. The existence of this phase is assumed owing to the Fe content in the ERNiFeCr-2 filler metal, which enhances the formation of this phase.

Despite of the annealing before the aging treatment, it is not possible to avoid the Nb partition because the solid-state diffusion is insignificant for this element. In virtue of this, an important number of carbides nucleate and grow in the HAZ and FZ limiting thus the precipitation of the hardening γ'' phase. These metallurgical mechanisms prevent to achieve the mechanical strength of the hardened IN718 alloy in the welded joints.

Acknowledgements The financial support given by the National Council of Science and Technology of the Mexican government to this project is acknowledged. The authors are grateful with the technical support given by Instituto de Investigación en Metalurgia y Materiales/UMSNH and the Centro de Investigación e Innovación Tecnológica/IPN.

References

1. DuPont JN, Lippold JC, Kiser SD (2011) Welding metallurgy and weldability of nickel-base alloys. John Wiley & Sons, Hoboken
2. Mortezaie A, Shamanian M (2014) An assessment of microstructure, mechanical properties and corrosion resistance of dissimilar welds between Inconel 718 and 310S austenitic stainless steel. Int J Pres Ves Pip 116:37–46. https://doi.org/10.1016/j.ijpvp.2014.01.002
3. Devendranath Ramkumar K, Patel SD, Sri Praveen S, Choudhury DJ, Prabaharan P, Arivazhagan N, Xavior MA (2014) Influence of filler metals and welding techniques on the structure–property relationships of Inconel 718 and AISI 316L dissimilar weldments. Mater Design 62:175–188. https://doi.org/10.1016/j.matdes.2014.05.019
4. Hirose A, Sakata K, Kobayashi KF (1998) Microstructure and mechanical properties of laser beam welded Inconel 718. Int J Mater Prod Technol 13(1–2):28–44
5. Hinojos A, Mireles J, Reichardt A, Frigola P, Hosemann P, Murr LE, Wicker RB (2016) Joining of Inconel 718 and 316 stainless steel using electron beam melting additive manufacturing technology. Mater Design 94:17–27. https://doi.org/10.1016/j.matdes.2016.01.041
6. Padilha AF, Rios PR (2002) Decomposition of austenite in austenitic stainless steels. ISIJ Int 42(4):325–337
7. Hirose A, Sakata K, Kobayashi KF (1997) Paper presented at the solidification processing 1997. Sheffield, UK
8. ASTM (2004) Standard test methods for tension testing of metallic 481 materials [metric]. vol ASTM E8M-04. ASTM International
9. ASTM (2016) Standard test method for tensile strain-hardening 483 exponents. vol ASTM E646-16. ASTM International
10. ASTM (2002) Standard test methods for notched bar impact testing 485 of metallic materials. vol ASTM E23-02. ASTM International
11. ASTM (2015) Standard test method for instrumented impact testing of metallic materials. vol ASTM E2298-15. ASTM International,
12. Mahajan S, Pande CS, Imam MA, Rath BB (1997) Formation of annealing twins in f.c.c. crystals. Acta Mater 45(6):2633–2638. https://doi.org/10.1016/S1359-6454(96)00336-9
13. Cieslak M (1991) The welding and solidification metallurgy of alloy 625. Weld J 70(2):49s–56s
14. Cieslak MJ, Headley TJ, Knorovsky GA, Romig AD, Kollie T (1990) A comparison of the solidification behavior of Incoloy 909 and Inconel 718. Metall Trans A 21(1):479–488. https://doi.org/10.1007/BF02782428
15. Cieslak MJ, Headley TJ, Romig AD, Kollie T (1988) A melting and solidification study of alloy 625. Metall TransA 19(9):2319–2331. https://doi.org/10.1007/BF02645056
16. Chalmers B (1964) Principles of solidification. Wiley, New York
17. Savage WF, Lundin CD, Aronson AH (1965) Weld metal solidification mechanics. Weld J 44:175–181
18. Dupont J, Banovic S, Marder A (2003) Microstructural evolution and weldability of dissimilar welds between a super austenitic stainless steel and nickel-based alloys. Weld J 82(6):125
19. Brooks J, Bridges P (1988) Metallurgical stability of Inconel alloy 718. Superalloys 88:33–42

20. Kou S (2003) Precipitation-hardening materials II: nickel base alloys. In: Welding metallurgy, 2nd edn. Wiley Interscience, New Jersey, pp 375–392
21. Rodriguez P (1984) Serrated plastic flow. B Mater Sci 6(4):653–663
22. Hong S-G, Lee S-B (2005) Mechanism of dynamic strain aging and characterization of its effect on the low-cycle fatigue behavior in type 316L stainless steel. J Nucl Mater 340(2–3):307–314. https://doi.org/10.1016/j.jnucmat.2004.12.012
23. Meng LJ, Sun J, Xing H, Yu WW, Xue F (2011) Study of low-cycle fatigue of AL6XN austenitic stainless steel. Nucl Eng Des 241(8):2839–2842. https://doi.org/10.1016/j.nucengdes.2011.06.011
24. James L (1978) Fatigue-crack growth in Inconel 718 weldments at elevated temperatures. Weld J Res Suppl 57(1):17s–23s